Eur. Phys. J. Plus (2021) 136:116
https://doi.org/10.1140/epjp/s13360-020-01056-6

THE EUROPEAN PHYSICAL JOURNAL PLUS

Regular Article

Impact of Bi_2O_3 modifier concentration on barium–zincborate glasses: physical, structural, elastic, and radiation-shielding properties

K. A. Naseer[1], **K. Marimuthu**[1,a], **K. A. Mahmoud**[2,3], **M. I. Sayyed**[4,5]

[1] Department of Physics, Gandhigram Rural Institute – Deemed to be University, Gandhigram 624 302, India
[2] Ural Federal University, St. Mira, 19, Yekaterinburg, Russia 620002
[3] Nuclear Materials Authority, Maadi, Cairo, Egypt
[4] Department of Physics, Faculty of Science, Isra University, Amman, Jordan
[5] Department of Nuclear Medicine Research, Institute for Research and Medical Consultations (IRMC), Imam Abdulrahman bin Faisal University (IAU), Dammam, Saudi Arabia

Received: 17 October 2020 / Accepted: 26 December 2020

Abstract A sequence of Bi_2O_3 varying barium–zincborate (BZX) glasses with the chemical composition (60-x) B_2O_3-20ZnO-20$BaCO_3$-$x$$Bi_2O_3-0.5Dy_2O_3$ (where $x = 0$, 5, 10, 15, 20, 25, and 30 in wt%) is fabricated by melt-quenching method. The fabricated samples were examined for the variation in physical, structural, elastic, and radiation-shielding properties with the Bi_2O_3 concentration. The structural and compositional evaluations are done using XRD and FTIR spectra. The BZX matrixes consist of the trigonal-planar and tetrahedral groups of borates, BiO_3 and BiO_6 units of Bi_2O_3, and the non-bridging oxygen in general. The average single-bond strength values substantiate the increasing ionic nature of the BZX glasses. The variation in the density and molar volume of the BZX series discussed in terms of various structural and elastic properties. The glass-coded BZ15 was found to be the best candidate for the sound-resistant applications based on the atomic packing fraction and the acoustic impedance studies. With MCNP5 simulation, the mass attenuation coefficient (MAC) values of all the samples were calculated and compared with a theoretical approach using the XCOM program. As the amount of Bi_2O_3 increases, the linear attenuation coefficient (LAC) increases with it at all energies. The LAC values varied between 0.2805 and 0.5269 cm^{-1} for the investigated glasses at 0.81 MeV. BZ30 glass is the more effective shield due to the highest MAC and LAC values.

1 Introduction

The global populace is growing, and the drastic industrialization in developing nations multiplied humankind's strive after energy by an exceptional amount. The more significant part of our energy originates from petroleum derivatives dig out from deep inside the Earth's crust. Over the past centuries, fossil fuels' use elevates the greenhouse gas level in the atmosphere, which is inextricably linked with climate change like global warming. The scientists around

[a] e-mail: mari_ram2000@yahoo.com (corresponding author)

Published online: 22 January 2021

the globe are unanimously challenging the people to wean off the fossil fuel habit. One of the tremendous difficulties the planet facing is this transformation toward a clean energy source which can slash the CO_2 emission. We have several renewable energy sources like solar energy, wind energy, tide energy, etc. But the problem is the amount of energy we are using in our day-to-day life is more than a million tera-joules. Even the largest nuclear power plant (NPP) (Kashiwazaki-Kariwa NPP) cannot provide that much energy in around five years. One of the solutions to meet this energy requirement is to build several NPPs, but NPPs are always at stake because of the safety concern. Some developed countries like Japan and Germany have decided to shut down their nuclear industry after Fukushima's tragic disaster in 2011 [1]. And many countries have turned down the appraisal for replacing the existing reactors. The world is moving on from Fukushima now and looking for improved NPP designs. The commercial NPP industry started flourishing again as a solution for the long-known reality of the rising energy demand. 'NuScale Power,' a company in the USA, introduced a new NPP design called small modular reactor (SMR), the next generation of NPP. The company managed to pass the fourth phase of the review of SMR by the US Nuclear Regulatory Commission, which is their first of a kind certification. The rest of the world is not different from this. Russia has already commenced a floating SMR in the Arctic Ocean; China announced SMR projects years before, and the UK also invested in a vast amount of money in SMR projects [2, 3].

Despite being small-sized, SMR also may go through similar issues as its bigger versions, particularly safety issues. There comes the relevance of research activities related to shielding materials. Nowadays, nuclear energy has a crucial role not only in energy production but also in medical, national security, and agricultural applications. The technicians and the people around the area are under immense threat of radiation exposure. As in any other industry, the mishaps in the nuclear industry also can be avoided or reduced to a minimal level by accurate designing and implementation. Despite being the source of skepticism, most of the scientists around the globe are working hard for making the nuclear industry a safer place. They keep on working on the safer NPP designs and trying to invent advanced protective layers for those who are related to the industry. To be protected from these extremely penetrating and ionizing radiations like X-rays and gamma-rays (γ–rays) is a grand challenge in this industry. For that, the NPP should be covered by a solid fence which can weaken the dosage of radiation under the secure line.

For a nuclear reactor, we should have some primary components which include the fuel material, structural materials, moderators, coolants, and finally the control, shielding, and safety materials. These materials should have specific properties which can be classified into two categories. Firstly, the general properties include structural, elastic, and mechanical properties along with reproducibility. The second one is the unique properties like radioactivity. Regardless of the fuel materials which must have unique properties, the different components of the reactor need a different kind of properties. The structural materials are aiding the exchange of the power between the core and the external system. These materials should have the properties like high melting point, high strength to weight ratio, good thermal stability, good corrosion resistance, high thermal neutron scattering, low vapor pressure, deficient thermal neutron absorption, etc. The moderators and reflectors are sharing the same set of properties which include high neutron scattering cross section, a large energy loss by a neutron per collision, and a low neutron absorption cross section. The high neutron scattering cross section of the moderators and reflectors helps to reduce the neutron leakage and escape. The properties of the blanket materials in a fast reactor are quite different from those for moderators and reflectors in a thermal reactor. The blanket materials should have a high neutron

absorption cross section. In addition to the nuclear requirements, these materials should be cost-effective, corrosion resistance, non-toxic, and ductile [4, 5].

Theoretically, a material with a critical density can decrease the radiation intensity, which makes them a shielding material. But based on the magnitude of energy, type of radiation, and the risk of exposure, shielding materials should be decided in advance. The conventional way of shielding the hazardous radiations involves building profound thick concrete barriers and using lead plates. Many scientists tried to improve the radiation protection efficiency of these concretes by mixing with minerals or changing the grain size [6, 7]. Similarly, the evaluation of radiation protection capacity of several alloys composites and polymers is also on the run [8–10]. In any case, these materials and techniques have downsides. For instance, these materials are not see through. Concrete walls are inclined to have cracks; once fixed, we can almost consider it as immobile, and the constituents can be different in a different part. Additionally, the world could be a better place if we reduce the usage of poisonous materials like lead (Pb). Like in any other industry, the nuclear industry also realized the potential applications of the glasses. Glasses have several advantages, and it has been a part of our culture for thousands of years. They can be used as a shielding material as well as storage for the nuclear wastes. Glasses are comfortable with making, clean, and transport. It can be tested for the impact of different constituents. It has corrosion resistance, could be cost-effective and transparent, which is a unique characteristic. The different factors of glass, such as the formers, modifiers, and intermediates, could be different according to their purposes [11–20]. The competence of glass to prevent hazardous radiation is inextricably linked with its composition. It should contain heavy-metal oxide (heavy-MO) in ample concentrations to stabilize the shielding properties with optical and mechanical properties. It is a prerequisite consideration in the glass making. Likewise, for the sensible handling of the hazardous rays, it is necessary to know the photon interaction parameters (PIP) like mass attenuation coefficient (MAC), half-value thickness ($\Delta_{0.5}$, or HVL), transmission factor (TF), and radiation protection efficiency (RPE) [18].

Among the different glass formers, borates have some unique properties. It has a considerable low melting temperature, high transparency, and the highest glass-forming affinity which does not crystallize even with slow cooling. The borate glasses are not an optimal candidate for γ radiation shielding (γ–RS) or other protective purposes in its pure form owing to its low chemical durability due to high water affinity. Hence for practical purposes, the metal oxides like SiO_2, TeO_2, PbO, BaO, ZnO, Bi_2O_3, etc., will add to the borate according to the purposes [17]. ZnO is an excellent candidate for giving stability for the borate glasses at a low cost. Also, the non-poisonous nature makes it an eco-friendly ingredient. Excess non-bridging oxygen (non-BO) formation causes when ZnO breaks the BO_4 units with the capacity of a network modifier [14, 16, 21]. Glasses having barium are an excellent preference for radioactive liquid waste disposal owing to its sulfate abiding capacity. It can be used as a barrier in plasma display ribs and as a γ–RS material [12, 16, 18, 19]. Both barium and zinc can be lowering the glass-forming temperature of the borates, even without a cluster formation [11]. Bi^{3+} is a massive, stable, and nonradiative nucleus. Owing to the lower field strength of Bi^{3+}, Bi_2O_3 can act as a conditional network former. Bismuth borate glasses have a relatively large thermal expansion coefficient, low optical dispersions, and low glass transition temperatures.

Recently, various binary, ternary, and poly borate glasses are evaluated for their structural and γ–RS properties. M. Rashad et al. [12] analyzed the PIP values and optical properties of barium lithium borate glasses. M.G.Dong et al. [20] employed simulation techniques to evaluate the change in different PIP of various glass systems, formed by silicates, tellurites, and borates, with germanate as the modifier. I. Boukhris et al. [13] and M.H.A. Mhareb et al.

[16] worked on zincborate glasses for the γ–RS characteristics. And G. Lakshminarayana et al. [15] dealt with the impact of bismuth oxide in γ–RS characteristics of the binary and ternary glasses employing the theoretical and computational approaches. Based on the above facts and figures, it is acceptable to investigate the glasses for radiation protection. And also, the essential properties of the glasses like optical transparency, stress and breakage strength, heat resistance, and chemical durability are expected for the selected composition from the literature review. Hence, it is sensible and worthy of the investigation of a series of barium–zincborate through a four-phase analysis (physical, structural, elastic, and γ–RS) by varying the concentration of bismuth oxide.

2 Materials and methods

2.1 Synthesis of Bi^{3+} varying barium–zincborate glasses

A faction of bismuth barium–zincborate (BZX) glasses is fabricated by the melt-quenching technique using analytical grade, 99.99% pure chemicals supplied by Sigma-Aldrich (B_2O_3, ZnO, $BaCO_3$, Bi_2O_3, and Dy_2O_3) [22]. In the present study, about 15 gm batches of chosen composition were weighed up and thoroughly ground using the agate mortar. This mixture is then made to melt in an electric furnace at 1025 °C for 55 min. During melting, the crucible containing mixture should be stirred two or three times to obtain homogeneity. Keep the brass mold preheated, and the molten mixture is poured into it and afterward by annealing at 350 °C for 12 h, for removing the thermal strain and bubbles and for improving the mechanical strength. The obtained glasses were polished to achieve plane surface, which will help to get better optical measurements. The chemical compositions (in wt%) used for the preparation of BZX glasses and the corresponding glass codes are given in Table 1. The glasses are coded BZ00-BZ30 depending on their Bi_2O_3 content in weight percentage. The $BaCO_3$, ZnO, and Dy_2O_3 content in the glasses remains the same for all the samples. The densities of the glasses have been calculated using the Archimedes principle, in which xylene is an immersion liquid. The refractive index estimation is done by Abbe's refractometer with mono-bromonaphthalene as the contact liquid, at 589.3 nm. For obtaining XRD and FTIR spectra, the authors employed similar types of equipment reported in Ref. [22] and performed at room temperature only.

2.2 Radiation-shielding characteristics

The standard way to determine the radiation-shielding ability of these glass samples is to conduct an experimental study calculating various parameters. However, due to the COVID-19 pandemic, laboratories are currently closed for operation. To circumvent this inconvenience while continuing to carry out investigations, simulations are used as an alternative method for experiments. Monte Carlo N-Particle Transport (MCNP) code is a commonly used simulation to determine the linear (LAC) and mass attenuation coefficient (MAC) of a sample based on the prediction of the average tack length (ATL) of gamma-photons in its pathway inside the glass sample. MCNP code was used to evaluate the gamma-photons' track length inside the fabricated glass samples. To achieve the required simulation, an input file was arranged. The mentioned input file contains a detailed description of the attenuator material, detector, and gamma-source, as shown in Fig. 1. A gamma-ray source emits photons with energies varied between 0.248 and 1.406 MeV along the Z direction in the present work. The radioactive source was placed in the center of the arranged geometry and 15 cm far from

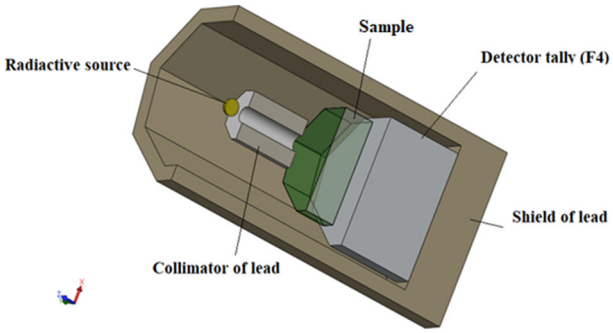

Fig. 1 The geometry and simulation setup

the fabricated glass sample. The emitted photons were collimated using a collimator of lead with a slit 1 cm in diameter. The collimator diameter 7 cm and height 10 cm. the collimated photons incident on the glass sample. The chemical composition and density of the fabricated glasses are illustrated in Table 1. According to the input file, the glass samples were in the form of a cylinder with a diameter of 2 cm and different thicknesses. After the interaction between the incident photons and the fabricated glass, the transmitted photons incident on the detector. The detector and the sample were in contact without any separating distance. The detector was assumed to be F4 tally, to record the track length of the incident photons per unit cell of the detector. The geometry was shielded from the surrounded environment by 5 cm of lead. The importance card was set up to be 1 for the cells inside the geometry and 0 for cells outside the geometry. Also, the NPS card was set up to stop the interaction after 10^6 histories. Continuous-energy nuclear and atomic data libraries support the MCNP code. The primary cross-sectional data sources for the MCNP-5 nuclear database are ENDF, ACTI, ENDL, ACTI, and T-16 files [23].

Moreover, the predicted ATL was used to calculate the critical shielding parameters such as half-value thickness ($\Delta_{0.5}$), transmission factor (TF), and radiation protection efficiency (RPE) according to the following relations [24].

$$\mathrm{LAC} = \frac{1}{x} \ln\left(\frac{I}{I_o}\right) \tag{1}$$

$$\mathrm{LAC} = (\mathrm{MAC}) * \rho \tag{2}$$

$$\Delta_{0.5} = \frac{\ln(2)}{\mathrm{LAC}} \tag{3}$$

$$\mathrm{TR}(\%) = e^{-\mathrm{LAC}} \tag{4}$$

$$\mathrm{RPE}(\%) = \left(1 - e^{-\mathrm{LAC}}\right) * 100 \tag{5}$$

where w_i and $(\mathrm{MAC})_i$ define the fractional weight and the mass attenuation coefficient of constituting elements, respectively.

Table 1 Composition, corresponding glass code, density (ρ), refractive index (n_d), average molecular weight (M_{av}), molar volume (V_m), and molar refractivity (R_m) of bismuth zincborate (BZX) glasses

Sl. no.	Chemical compositions (in wt%)	Glass codes	ρ (g/cm^3)	n_d	M_{av} (g/mol)	V_m (cm^3/mol)	R_m (cm^3/mol)
1	60 B_2O_3-20 $BaCO_3$-19.5 ZnO-00 Bi_2O_3-0.5 Dy_2O_3	BZ00	4.114	1.526	98.980	24.061	7.386
2	55 B_2O_3-20 $BaCO_3$-19.5 ZnO-05 Bi_2O_3-0.5Dy_2O_3	BZ05	4.768	1.578	118.797	24.918	8.269
3	50 B_2O_3-20 $BaCO_3$-19.5 ZnO-10 Bi_2O_3-0.5Dy_2O_3	BZ10	5.520	1.636	138.614	25.111	9.002
4	45 B_2O_3-20 $BaCO_3$-19.5 ZnO-15Bi_2O_3-0.5 Dy_2O_3	BZ15	6.084	1.692	158.431	26.039	9.975
5	40 B_2O_3-20 $BaCO_3$-19.5 ZnO-20Bi_2O_3-0.5 Dy_2O_3	BZ20	6.523	1.725	178.248	27.326	10.850
6	35 B_2O_3-20 $BaCO_3$-19.5 ZnO-25Bi_2O_3-0.5 Dy_2O_3	BZ25	6.874	1.751	198.065	28.813	11.751
7	30 B_2O_3-20 $BaCO_3$-19.5 ZnO-30Bi_2O_3-0.5 Dy_2O_3	BZ30	7.161	1.779	217.882	30.425	12.753

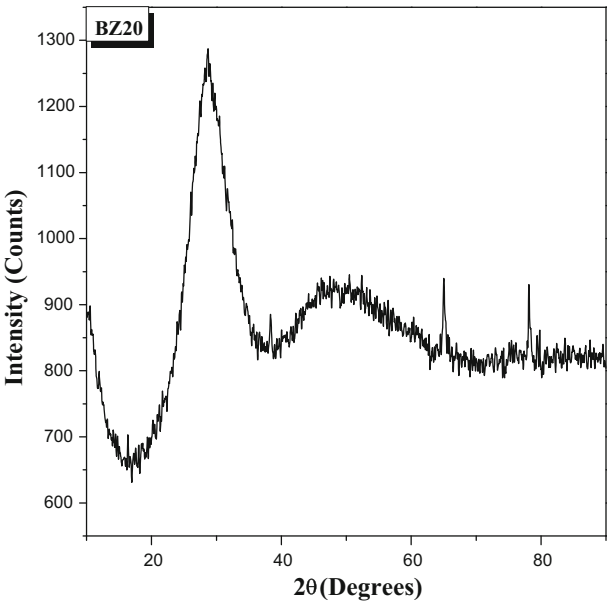

Fig. 2 XRD pattern of the 20 wt% Bi_2O_3 contain barium–zincborate glass

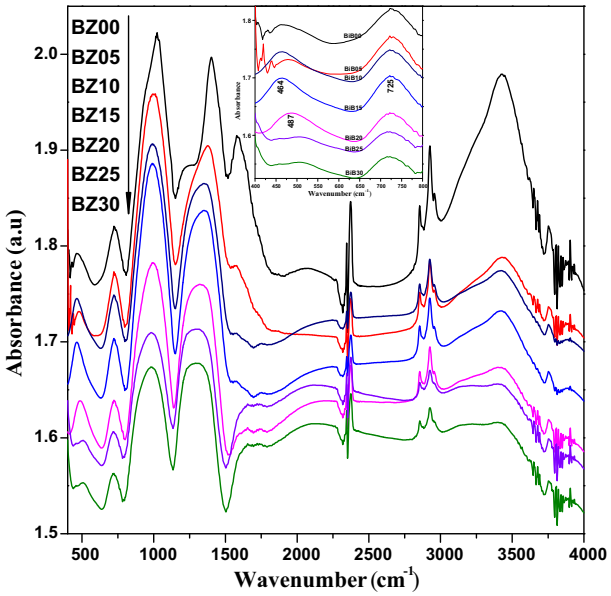

Fig. 3 Infrared absorbance spectra of the BZX glass

3 Results and discussions

3.1 Physical properties

The physical properties of the BZX glasses are evaluated following the previous work [22] and displayed in Table 1. The density (ρ) of the BZX glasses shows an augmentation. As the Bi_2O_3 amount is increased, the oxide replaces the lighter B_2O_3 present, which is increasing the glass density. The glass samples are arranged in the order of increasing density. From BZ00, having a density of 4.114 g/cm^3 to BZ30, having a density of 7.161 g/cm^3. The factors like glass structure compactness, geometrical configuration changes, and the interstitial spatial dimensions of the glass and coordination number will affect the density of the glass. The addition of Bi_2O_3 into the host matrix will change the tetragonal BO_4 groups into the triangular BO_3 groups by the formation of non-BO, and when the number of non-BO increases the density of the glass also increases. Similarly, the refractive index (n_d) also showed an escalated trend, 1.526 to 1.779, with increasing concentration of Bi^{3+}; seem to be dependent on the increasing number of non-BO. The refractive index and density are found to be linearly proportional, hence increase with an increase in the number of non-BO [22]. The molar volume (V_m) of the glasses follows the same trend as ρ, which might be a sign of the structural changes of the glasses like an increase in the non-BO bond density. Generally, n_d relies on the composition of the glass as the polarizability of the non-BO is higher than that of bonding ones [11]. An elevated value of molar refractivity (R_m) with increasing concentration of Bi^{3+} confirms the creation of non-BO in the glasses. Decreasing metallization (M) and energy-gap ($E_g[n_d]$) values with increasing Bi^{3+} is a sign of the nonmetallic nature of the BZX glasses [18, 25].

$$M = 1 - \left(\frac{R_m}{V_m}\right) \tag{6}$$

3.2 Structural examination

The XRD spectrum of the BZ20 glass (Fig. 2) is documented in the range $10^\circ \leq \theta \leq 90^\circ$. The analyzed sample's amorphous nature is confirmed from the spectrum, as there are no sharp peaks [26]. The existence of nucleation will generate sharp peaks in the spectrum. We can expect the same amorphous nature for the rest of the glasses in the BZX series as the methodology followed is exactly alike at a similar laboratory environment. Figure 3 portrays the FTIR absorbance spectra recorded in the region 400–4000 cm^{-1} of the BZX samples. The absorption in the lower-energy region is very much essential for the confirmation of metal–oxygen bonds. And the same is portrayed as an enlarged inset image. The band assignments of each peak in the spectra are enlisted in Table 2. The various functional groups presented in a borate glass matrix are BO_3 units, BO_4 units, boroxyl rings, etc. All these are active in their respective active IR areas [18, 27]. In the low-order glasses, the metal-oxide bonds are presented at 460 cm^{-1}, whereas the bands are shifted toward 490 cm^{-1} in the higher-order glasses due to the internal structural changes. IR absorption of CO_2 is presented at 2370 cm^{-1} due to the measuring conditions/errors [18].

3.3 Structural properties

The structural characteristics of the BZX glasses are evaluated by making use of the expressions used in previous work [18] and given in Table 3. The boron–boron separation [r(B–B)] and bismuth–bismuth separation [r(Bi–Bi)] will provide information about the

Table 2 Band positions (in cm^{-1}) and the corresponding peak assignments of FTIR spectra of BZX glasses

BZ00	BZ05	BZ10	BZ15	BZ20	BZ25	BZ30	Assignments
464	474	464	464	–	–	–	Vibrations of Bi–O in BiO_6 octahedral units/Specific vibrations of Ba–O bonds
–	–	–	–	487	504	506	Symmetry bending vibrations of BiO_3 units/Specific vibrations of Ba–O bonds low intensity
725	726	724	725	724	719	718	B–O–B bending vibrations in borate network
1024	1003	986	997	981	989	981	B–O stretching vibration of BO_4 units in tri-, tetra- and pentaborate groups
1403	1376	1349	1322	1335	1352	1304	B–O stretching vibration of BO_3 units in meta, pyroborate and orthoborate groups
1586	1580	1582	1599	1623	1580	1655	B–O stretching vibration of isolated pyroborate group
2373	2373	2374	2375	2374	2370	2375	IR absorption of CO_2
2854	2855	2855	2854	2852	2850	2855	Hydrogen bonding
2925	2925	2927	2924	2926	2927	2924	
3426	3429	3423	3412	3418	3445	3436	Fundamental stretching of O–H group
3752	3752	3752	3753	3753	3756	3756	

Table 3 Structural properties of the BZX glasses

Structural Properties	BZ00	BZ05	BZ10	BZ15	BZ20	BZ25	BZ30
Metallization criterion, M	0.693	0.668	0.642	0.617	0.603	0.592	0.581
The boron–boron separation, r(B–B) (Å)	4.127	4.061	3.958	3.892	3.838	3.787	3.733
Distribution density of B, $D_{d(B)}$ ($\times 10^{-13}$ $m^{-2}mol^{-1}$)	1.715	1.630	1.576	1.494	1.404	1.314	1.227
The bismuth–bismuth separation, r(Bi–Bi) (Å)	2.713	2.754	2.771	2.816	2.874	2.941	3.013
Distribution density of Bi, $D_{d(Bi)}$ ($\times 10^{-13} m^{-2}mol^{-1}$)	1.128	1.105	1.103	1.081	1.052	1.021	0.990
Oxygen packing density, OPD (g atom/cm^3)	108.47	104.74	103.94	100.23	95.51	90.58	85.78
Molar volume of oxygen, Vo (cm3/mol)	9.887	10.368	10.596	11.166	11.935	12.856	13.918
Average coordination number, m	3.455	3.507	3.566	3.631	3.705	3.789	3.884
Number of bonds per unit volume, n_b ($\times 10^{22}$ m^{-3})	8.648	8.477	8.552	8.399	8.166	7.919	7.690
Average single-bond strength of the glasses, $B_{M\text{-}O}$ (KJ/mol)	308.57	302.65	296.06	288.68	280.37	270.92	260.09
Optical band gap, E_g [n_d] (eV)	4.126	4.042	3.948	3.858	3.805	3.763	3.718
Two-photon absorption coefficient, β (cm/GW)	3.341	3.920	4.678	5.410	5.841	6.180	6.546

compactness of the glasses. The average values of these separations rely on the molar volumes of boron (B) [V_m^B] and bismuth (Bi) [V_m^{Bi}] which are strongly interconnected to their ionic radii.

$$r(\mathrm{B{-}B}) = \left(\frac{V_m^B}{N_A}\right)^{1/3} \tag{7}$$

$$r(\mathrm{Bi{-}Bi}) = \left(\frac{V_m^{Bi}}{N_A}\right)^{1/3} \tag{8}$$

$$V_m^B = \frac{V_m}{2(1 - X_B)} \tag{9}$$

$$V_m^{Bi} = \frac{V_m}{2(1 - X_{Bi})} \tag{10}$$

where X_B and X_{Bi} are the molar fractions of boron and bismuth, respectively, and N_A is the Avogadro number. The r(B–B) values decrease with increase in concentration of Bi^{3+} due to the insertion of Bi^{3+} into the network, which has a larger ionic radius. On the other hand, the r(Bi–Bi) values are increasing as the Bi^{3+} goes higher, owing to a higher V_m. Hence, the compactness of the glass matrix can only be deep-rooted by the analysis of the distribution density (D_d). The D_d of a species is the ratio of the separation between the same to the molar volume of the glass.

$$D_{d(B)} = \frac{r(\mathrm{B-B})}{V_m} \tag{11}$$

$$D_{d(Bi)} = \frac{r(\mathrm{Bi-Bi})}{V_m} \tag{12}$$

The D_d of both B and Bi shows a descending trend even with higher Bi^{3+} concentration which shows the increasing compactness of the higher-order glasses. Figure 4 illustrates the deviation of D_d with the Bi^{3+} concentration. The oxygen packing density (OPD) and the molar volume of oxygen (V_o) are in the reverse tendency.

$$\mathrm{OPD} = \frac{\rho_{glass} * N_A * \text{Number of oxygen}}{M_{av}} \tag{13}$$

$$V_O = \frac{V_m}{\sum_i (x n_o)_i} \tag{14}$$

where x_i is the molar fraction of each component i, and n_o is the number of oxygen atoms in each constituent oxide.

The OPD is dropping off with higher Bi^{3+} concentration, while the V_o has a substantial growth, and Fig. 5 gives the graphical demonstration. The above two statements simultaneously are pointing out an increase in non-BO. The bond density (n_b) of any matrix will be altered by incorporating a heavy-metal ion like Bi^{3+}. And n_b showing a negative trend with the Bi^{3+} concentration.

$$n_b = \frac{N_A}{V_m} \sum_i (x n_c)_i = \frac{N_A}{V_m} m \tag{15}$$

where m is the average coordination number, and n_c is the coordination number of the cation.

Hence, the augmentation in the V_m might be because of the structural changes in the network. Increased B–O vibrations might be the outcome of increased Bi^{3+} concentration. The average coordination number (m) can give us the metal–oxygen bond nature. And an increase in trend of 'm' with Bi^{3+} concentration proves the additional formation of non-BO

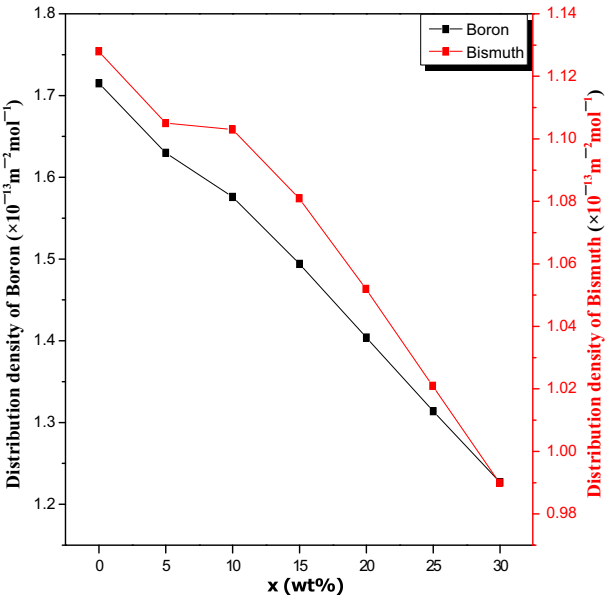

Fig. 4 Composition dependence of distribution densities of boron and bismuth of BZX glasses with respect to Bi_2O_3 concentration

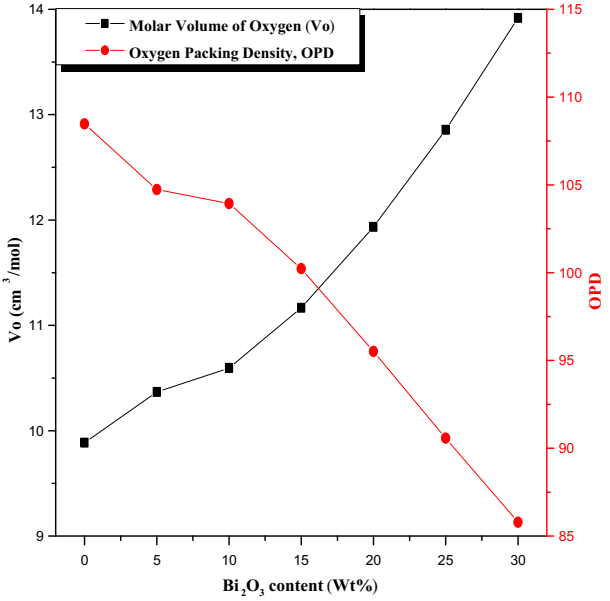

Fig. 5 The composition-dependent variation of the molar volume oxygen (V_o) and the oxygen packing density (OPD) of BZX glasses with increasing concentration of Bi_2O_3

and hence the existence of BO_4 units in the glass matrix. All the above results establish an enhanced cross-linking of the glass matrix with increasing concentration of Bi^{3+} [28]. The

average single-bond strength of the glasses ($B_{M\text{-}O}$) shows a demoted trend with the Bi^{3+} concentration. This might be the outcome of the formation of Bi–O–Bi units which have a higher ionicity [29]. The same is confirmed by the FTIR spectra of the BZX glasses. The two-photon-absorption coefficient (2PAC) can be estimated using the optical band gap. And a low-order 2PAC value makes the BZX glasses useful for the nonlinear optical applications [30].

$$\beta(\text{cm/GW}) = 36.66 - 8.1 \times E_g(\text{eV}) \tag{16}$$

3.4 Elastic properties

The pure borate network is laminar shaped, which consists of trigonal-planar borate units. Any addition that caused the breakage of trigonal-planar units to the tetrahedral borate units will create the non-BO, which helps to increase the connectivity of the glass matrix. Hence, the incorporation of Bi^{3+} into the glass matrix causes the breakage of B–O–B, which confirms the elevated V_m. Also, with the capacity of a network modifier, the addition of Bi^{3+} ended up in the formation of Bi–O–Bi bonds. It will increase the chemical durability and the thermal stability of BZX glasses. More Bi–O–Bi units will be introduced while increasing the Bi^{3+} concentration, which will alter the cross-link density ($Ł_d$) and thus condense the structure [31].

Various elastic moduli ($M_{elastic}$) and the Poisson's ratio (μ_{cal}) of the BZX glasses evaluated using the Makishima and Mackenzie model [32, 33] and enlisted in Table 4. The estimation is based on the packing density (C_g) of the composition as well as the bond dissociation energy (BDE) of the corresponding constituents. Obviously, there will be a change in the $M_{elastic}$ associated with a material phase change. The estimation of $M_{elastic}$ can provide information about the glass structure as they very much rely on nature and interatomic interactions of the chemical bond. Young's modulus (E_t) depends on the bond's nature, whereas the bulk modulus (K_t) measures the changes in the stretching force constant of the bond and $Ł_d$. From the mathematical expressions [31–39], it is evident that the $M_{elastic}$ increases with an increase in the velocity or density. For BZX glasses, even though there is an increase in the density, $M_{elastic}$ shows a converse trend. Hence for the BZX glasses, the network bond type has a crucial role in determining the $M_{elastic}$. The $M_{elastic}$, especially E_t is directly proportional to the C_g. With a demoted C_g, we can expect the reverse trend of $M_{elastic}$ with the V_m. Also, the C_g is in an inverse relation with V_m, and this also might be the reason for the reverse trend of $M_{elastic}$ [36]. The variation of theoretically calculated $M_{elastic}$ with V_m is graphically demonstrated in Fig. 6. The resistance provided by a material toward any permanent deformation or penetration refers to the microhardness (H_m). The variation in H_m is negligible for the BZX glasses.

The network compactness can be measured using another vital parameter known as atomic packing fraction (A_{PF}). A_{PF} is the ratio of the volume summation of atoms to the V_m. Even though the variation in the A_{PF} is nominal, the increase in trend is being reversed after BZ15. It could be because of the elevation in the fraction of tetrahedral borate units up to $x = 15$, which has a larger packing density. When the value of x goes further, there might be a creation of non-BO due to the structural change of borate units [40]. Acoustic impedance (Z) is a valuable property for portraying impacts that happen when the sound wave meets the boundary between two media. There is a certain likeness among the reflection

Table 4 Elastic properties of the BZX glasses

Elastic Properties	BZ00	BZ05	BZ10	BZ15	BZ20	BZ25	BZ30
Poisson's ratio, μ_{cal}	0.2032	0.2035	0.2039	0.2043	0.2047	0.2052	0.2058
Atomic packing fraction, A_{PF}	0.8772	0.9597	1.0430	1.0768	1.0741	1.0496	1.0054
Atomic packing density, Cg (10^{-6} m^{-3})	0.736	0.706	0.696	0.665	0.628	0.589	0.551
Acoustic impedance, Z (10^5 g cm^{-2} s^{-1})	12.2	12.76	13.49	13.7	13.61	13.33	12.92
Young's modulus, E_t (GPa)	36.21	34.14	32.98	30.85	28.38	25.84	23.32
Bulk modulus, K_t (GPa)	31.88	28.84	27.44	24.55	21.32	18.21	15.37
Shear modulus, S_t (GPa)	14.70	13.95	13.51	12.73	11.83	10.90	9.98
Longitudinal modulus, L_t (GPa)	51.47	47.43	45.45	41.52	37.09	32.75	28.67
Microhardness, H_m (GPa)	1.737	1.718	1.688	1.663	1.636	1.606	1.570
Fractal dimension, d_F	1.844	1.935	1.969	2.074	2.220	2.396	2.597
The average cross-link density, $Ł_d$	3.602	3.581	3.557	3.531	3.501	3.467	3.428
Average stretching force constant, $\dot{F}_s$ (N/m)	506	493	479	464	447	427	406

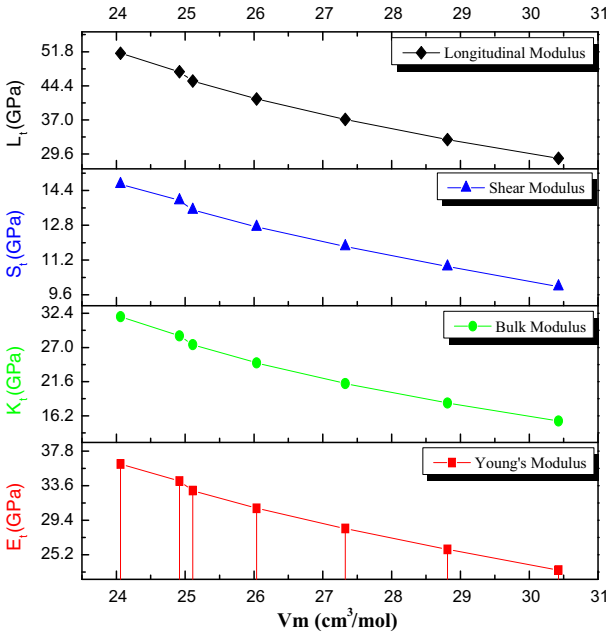

Fig. 6 The elastic moduli of the BZX glasses as a function of the molar volume (V_m) of the glasses

and transmission of longitudinal ultrasound and light through the phase boundaries. The transmitted intensity of the sound is related to Z as the following equation,

$$\frac{I_{\text{transmitted}}}{I_{\text{incident}}} \cong \left[\frac{Z_{\text{air}}}{Z_{\text{glass}}}\right]^2 \left[\frac{v_{\text{sound in glass}}}{\pi f d_{\text{glass}}}\right]^2 \tag{17}$$

where d is the glass thickness and f is the frequency. The larger the Z, the smaller the intensity transmitted. Like the A_{PF}, Z is also showing an increase in trend up to the BZ15.

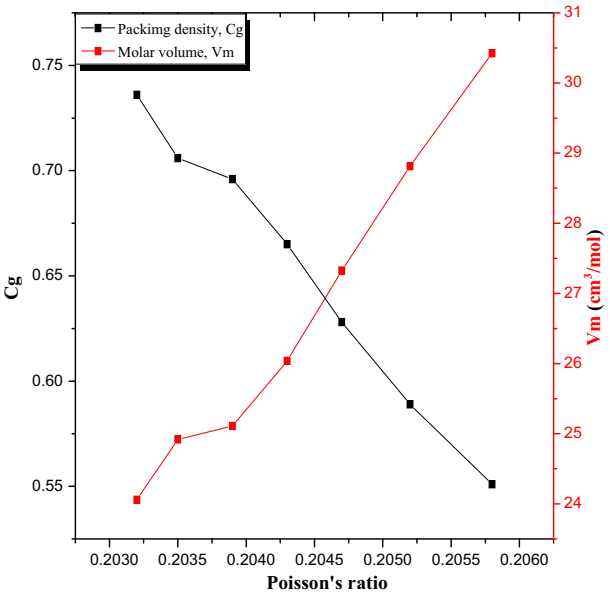

Fig. 7 The Poisson's ratio as a function of packing density (C_g) and the molar volume (V_m) of the BZX glasses

When a perpendicular tensile force is applied, the glass will experience a lateral-strain. And it will be maximum in the absence of bridging oxygen (BO). The more BO, which makes the network more cross-linking, the lateral strain will be minimized. The measure of this transversal enhancement concerning the axial compression is known as the Poisson's ratio (μ_{cal}). Taking up the C_g of the BZX glasses, μ_{cal} evaluated, and the relatively lesser values prove a high cross-linking density [41]. The graphical illustration of the dependence of μ_{cal} with V_m and C_g is portrayed in Fig. 7. The variation in the μ_{cal} caused a significant change in dimensionality, which is confirmed by the estimation of the fractal dimension (d_F). The d_F gives a valuable dimensionality picture of the matrix. For a 3D structure, d_F is 3 and 2 for the 2D network. From the evaluated values of d_F, it is evident that the dimensionality of the glass network changes from 2D to 3D. Hence, the Bi^{3+} addition makes the glass matrix hard and stress resistant. The average stretching force constant $\left(\dot{F}_s\right)$ showed a gradual reduction which might be owing to an increase in bond length or interatomic spacing.

3.5 Radiation attenuation characteristics

The MAC describes the ability for a material to attenuate radiation and is needed to compute other parameters, with a more excellent value signifying a better shield. With MCNP5 simulation, the MAC values of all the samples are various energies were calculated. The simulated MAC values were compared to the XCOM's values to determine the simulation process's accuracy. The theoretical values were obtained from the XCOM database [42]. The two methods are compared in Table 5. The two received values can be observed to be very close together for all seven glasses at all energies within an acceptable deviation. For instance, at 0.248 MeV, the BZ00 glass has a MAC equal to 0.1373 cm^2g^{-1} according to MCNP5, and a MAC of 0.1374 cm^2g^{-1}, according to XCOM. For the BZ30 glass at 1.406 MeV, its

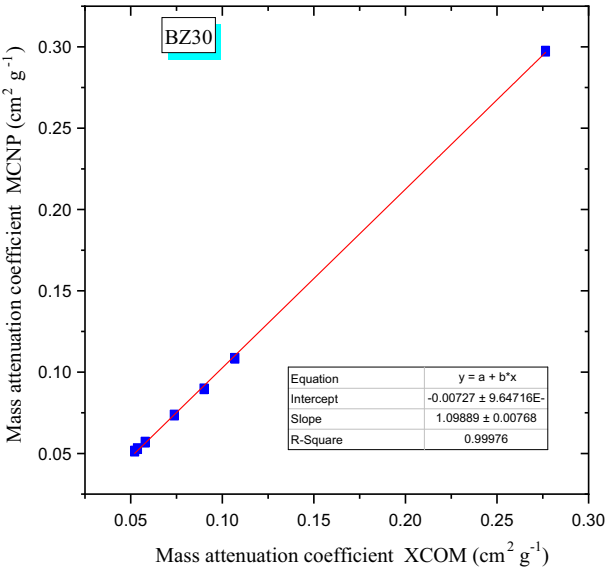

Fig. 8 Comparison between the simulated and calculated MAC

MACs are equal to 0.0514 and 0.521 cm^2g^{-1} based on MCNP5 and XCOM, respectively. The table accounts for differences in energies and composition of the glasses, and neither caused inaccuracies in the simulation. Finally, the correlation between the two values is determined in Fig. 8. When plotting and comparing the MAC values from both methods, the R-squared value was calculated to be practically one, which signifies that the methods agree with each other almost exactly. Therefore, based on these results, it can be confirmed that the MNCP5 code is an accurate method for determining the radiation-shielding ability of the tested samples.

With the MAC values calculated, other essential parameters were determined to evaluate the glasses further. The first of these is the linear attenuation coefficient or LAC. The LAC is attained by multiplying the MAC by the density of the sample, with the greater value being more desirable. Figure 9 illustrates a three-dimensional model of the LAC against energy and the Bi_2O_3 content in weight percentage. The influence of energy on the LAC can first be examined. The figure demonstrates that for all the glasses as energy increases, the LAC decreases. This trend occurs because as photons increase in energy, they can penetrate through the glass with greater ease, decreasing the probability of interaction and decreasing the LAC. This decrease, however, occurs in two phases. The first phase occurs at lower energies, where the LAC decreases sharply as energy increases due to the dominance of the photoelectric effect in this range. For instance, the LAC for BZ00 decreases from 0.5648 cm^{-1} to 0.3550 cm^{-1} when the energy increases from 0.248 MeV to 0.511 MeV. For BZ25, it decreases from 1.8733 cm^{-1} to 0.7087 cm^{-1} within the same energies. As energy increases further, the LAC rate decreases by slow down due to the photoelectric effect becoming less dominant. Instead, Compton scattering begins to become increasingly more prevalent. For example, BZ00 decreases from 0.2163 cm^{-1} to 0.2103 cm^{-1} and BZ30 decreases from 0.3793 cm^{-1} to 0.3683 cm^{-1} when the energy increases from 1.332 MeV to 1.406 MeV.

Next, the influence of the Bi_2O_3 content on the LAC is observed in Fig. 9. As the amount of Bi_2O_3 increases, the LAC increases with it at all energies. At 0.81 MeV, the LAC values

Table 5 The mass attenuation coefficient (cm^2/g) of the fabricated BZX glasses

Energy MeV	Mass attenuation coefficient ($cm^2\ g^{-1}$)													
	BZ00		BZ05		BZ10		BZ15		BZ20		BZ25		BZ30	
	MCNP	XCOM	MCNP	XCOM	MCNP	XCOM	MCNP	XCOM	MCNP	XCOM	MCNP	XCOM	MCNP	XCOM
0.248	0.1373	0.1374	0.1603	0.1606	0.1923	0.1838	0.2145	0.2069	0.2538	0.2301	0.2725	0.2533	0.2973	0.2765
0.511	0.0863	0.0864	0.0896	0.0898	0.0930	0.0932	0.0964	0.0966	0.0997	0.1001	0.1031	0.1035	0.1085	0.1069
0.662	0.0755	0.0781	0.0772	0.0801	0.0788	0.0821	0.0804	0.0840	0.0821	0.0860	0.0837	0.0880	0.0897	0.0900
0.81	0.0682	0.0683	0.0691	0.0692	0.0700	0.0701	0.0709	0.0711	0.0718	0.0720	0.0727	0.0729	0.0736	0.0738
1.173	0.0561	0.0565	0.0562	0.0567	0.0564	0.0569	0.0565	0.0572	0.0567	0.0574	0.0568	0.0577	0.0569	0.0579
1.332	0.0526	0.0529	0.0526	0.0530	0.0527	0.0532	0.0528	0.0533	0.0528	0.0534	0.0529	0.0536	0.0530	0.0537
1.406	0.0511	0.0514	0.0512	0.0515	0.0512	0.0517	0.0513	0.0518	0.0513	0.0519	0.0514	0.0520	0.0514	0.0521

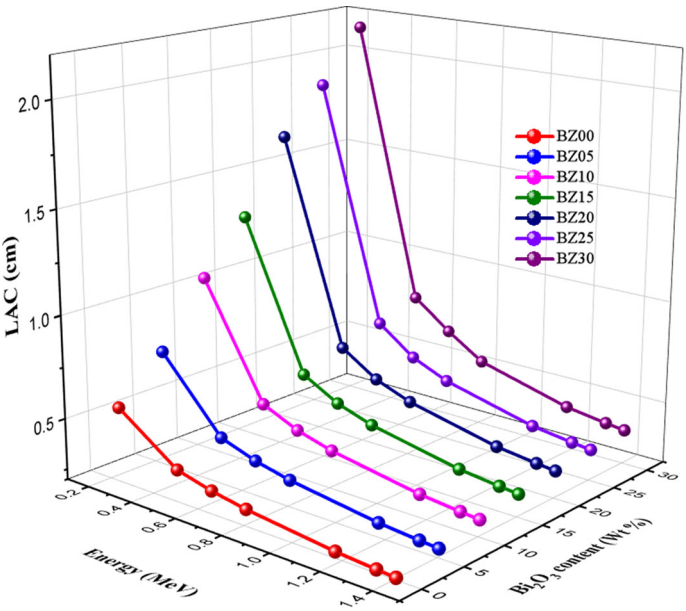

Fig. 9 The linear attenuation coefficient of BZX glasses

are equal to 0.2805, 0.3294, 0.3863, 0.4313, 0.4683, 0.4996, and 0.5269 cm^{-1} for BZ00, BZ05, BZ10, BZ15, BZ20, BZ25, and BZ30, respectively. This increase is caused by an increase in the glass density, as the weight of the Bi_2O_3 increases. Therefore, as the Bi_2O_3 content in the glasses increases, and the density along with it, the attenuation ability of the glasses increases as well. In can then be concluded that BZ30 is the more effective shield out of the investigated glasses at all the tested energies.

Another important radiation-shielding parameter is called the half-value layer (HVL), representing the thickness of a material required to reduce the intensity of the incoming radiation intensity in half, with a smaller thickness signifying a better shield. Figure 10 plots the HVL against energy and the Bi_2O_3 content in a three-dimensional diagram. All the HVL values can be observed to increase as energy increases. This trend occurs because as the energy of the incoming photons increases, the material needs to be thicker to reduce the intensity in half. For the BZ15 glass, the HVL increases from 0.5312 cm at 0.248 MeV, to 1.6072 cm at 0.81 MeV, and 2.2218 cm at 1.406 MeV. In terms of density, as the Bi_2O_3 content in the glasses increases, the HVL decreases. At 1.406 MeV, the HVL decreases from 3.2957 cm to 2.2218 cm to 1.8818 cm for BZ00, BZ15, and BZ30, respectively. These results indicate that increasing the amount of Bi_2O_3 in the glasses, and the density with it, decreases the HVL, increasing the performance of the glasses. Following the LAC, the HVL demonstrates that BZ30 has the best attenuation properties.

Figure 11 illustrates the transmission factor (TF), or transmission rate, of the glasses at three different thicknesses. The transmission factor is the ratio of the photons that passed through the sample to the total photons and is calculated as a percentage. Thicknesses of 0.5 cm, 1 cm, and 3 cm were chosen to evaluate the effect of the material thickness, thinner and thicker samples, on the TF. Four energies were selected, 0.511 MeV, 0.81 MeV, 1.173 MeV, and 1.406 MeV, to understand the effect of low and high energies on the TF. In subfigure [a], the TF for all seven glasses decreases as the material's thickness increases. This trend

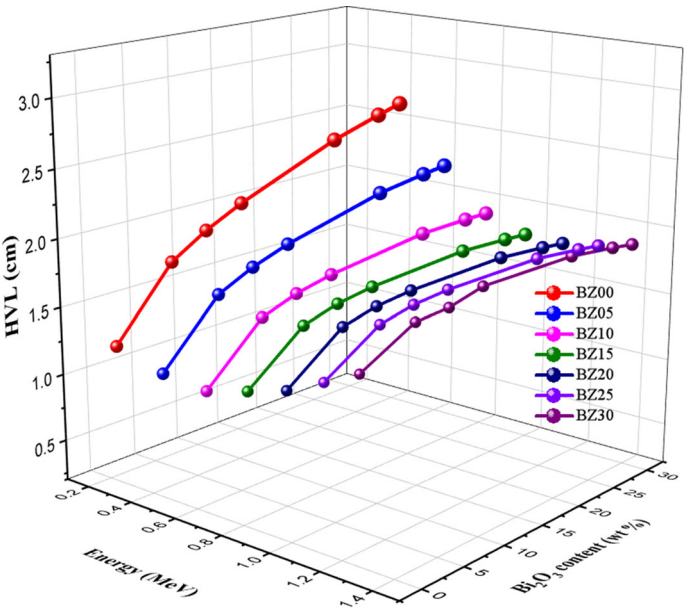

Fig. 10 Variation of the half-value layer versus the incoming photon energy and Bi_2O_3 content for the fabricated BZX glasses

occurs because as the thickness of the material increases, less photon can pass through the sample. Thus, the TF decreases for all fabricated samples. At energy 0.511 MeV, the TF of the BZ00 glass sample decreases from 83.74% at a thickness of 0.5 cm, to 70.12% at 1 cm, and 34.47% at 3 cm. Besides, it increases with the Bi_2O_3 content of the glasses at constant energy and decreases with the thicknesses of the sample. At 0.511 MeV and at a thickness of 1 cm, the TF is equal to 70.12%, 65.22%, 59.84%, 55.64%, 52.17%, 49.23%, and 45.99% for BZ00, BZ05, BZ10, BZ15, BZ20, BZ25, and BZ30, respectively. When observing a constant thickness but increasing energy, the TF increases for all seven glasses. For instance, the TF of BZ30 at 3 cm increases from 9.73% at 0.511 MeV, to 20.58% at 0.81 MeV, 29.43% at 1.173 MeV, and 33.21% at 1.406 MeV. This increase occurs because as the energy of the incoming photons increases, more radiation can pass through the material, increasing TF. This figure confirms that BZ30 has better shielding properties out of the investigated glasses.

Additionally, the glasses can perform better at lower energies, and their ability to shield radiation decreases as photon energy increases. Lastly, it can be concluded that the glasses perform significantly better when their thickness increases. Therefore, if space is not a significant concern, a thicker glass should be installed when using these samples.

4 Conclusion

The discrepancy of physical, structural, elastic, and radiation-shielding characteristics of a novel bismuth barium–zincborate glasses (BZX) with a chemical formula (60-x) B_2O_3–20ZnO–20$BaCO_3$–$x$$Bi_2O_3$–0.5$Dy_2O_3$ (x = 0, 5, 10, 15, 20, 25, and 30 in wt%) is analyzed and detailed. BZX series are fabricated using the conventional melt-quenching procedure without any bubbles. While increasing the concentration of Bi^{3+}, there is an aug-

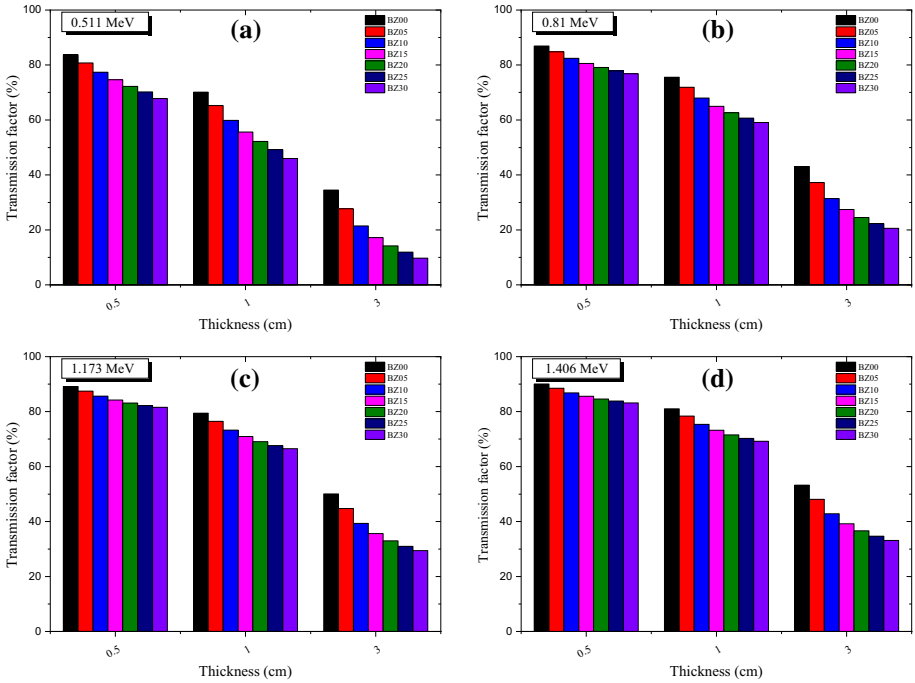

Fig. 11 Variation of the transmission rate versus the glass thickness at various gamma-photon energy

mentation in BO_4 units and the metal-oxide bonds, which will enhance the glass stability. So, the bismuth oxide acts as a network former in the present composition. The lowering trend of the average single-bond strength point toward an ionic nature of the BZX glasses and the low-order 2PAC is useful in the perspective of NLO applications.

The elastic moduli and the Poisson's ratio of the present BZX glasses are very much related to the network bond type rather than the density. Hence, downgrading is observed in the elastic moduli. The relatively lesser values prove an elevated cross-linking density. From the evaluated values of fractional dimension, it is obvious that the dimensionality of the glass network changes from 2D to 3D. With the MCNP5 simulation, the MAC values of all the seven samples were calculated to explore the possibility of using the current glasses as shielding materials. The LAC for BZ00 decreases from 0.5648 cm^{-1} to 0.3550 cm^{-1} when the energy increases from 0.248 MeV to 0.511 MeV and from 0.2163 cm^{-1} to 0.2103 cm^{-1} when the energy increases from 1.332 MeV to 1.406 MeV. The HVL results showed that as the energy of the incoming photons increases, the material needs to be thicker to reduce the intensity in half. Also, the HVL results indicate that increasing the amount of Bi_2O_3 in the glasses, and the density with it, decreases the HVL, increasing the performance of the glasses. BZX glasses are a better candidate for long-lasting radiation shielding in ventures like the

medical/industrial purpose PET/X-ray and NPP. The results acquired from the MCNP code are in excellent agreement with those from XCOM.

Compliance with ethical standards

Conflict of interest We have no conflict of interest to declare.

References

1. A. Brunnengräber, M. Schreurs, Nuclear Energy and Nuclear Waste Governance Perspectives after the Fukushima Nuclear Disaster, in: Nucl. Waste Gov., Springer Fachmedien Wiesbaden, Wiesbaden (2015), pp. 47–78. https://doi.org/10.1007/978-3-658-08962-7_2
2. L. Parshley, When It Comes to Nuclear Power, Could Smaller Be Better? Yale Sch. Environ. **3**, 15 (2020)
3. Application Review Schedule for the NuScale Design, U.S. Nucl. Regul. Comm. (2020). https://www.nrc.gov/reactors/new-reactors/smr/nuscale/review-schedule.html. Accessed 7 Aug 2020
4. B.M. Ma, Nuclear reactor materials and applications, Van Nostrand Reinhold, United States (1983)
5. C.K. Gupta, *Materials in Nuclear Energy Applications*, vol. II (CRC Press, London, 2018)
6. O. Agar, H.O. Tekin, M.I. Sayyed, M.E. Korkmaz, O. Culfa, C. Ertugay, Experimental investigation of photon attenuation behaviors for concretes including natural perlite mineral. Results Phys. **12**, 237–243 (2019). https://doi.org/10.1016/j.rinp.2018.11.053
7. O. Agar, Study on gamma ray shielding performance of concretes doped with natural sepiolite mineral. Radiochim. Acta **106**, 1009–1016 (2018). https://doi.org/10.1515/ract-2018-2981
8. O. Agar, M.I. Sayyed, F. Akman, H.O. Tekin, M.R. Kaçal, An extensive investigation on gamma ray shielding features of Pd/Ag-based alloys. Nucl. Eng. Technol. **51**, 853–859 (2019). https://doi.org/10.1016/j.net.2018.12.014
9. E. Şakar, Determination of photon-shielding features and build-up factors of nickel–silver alloys. Radiat. Phys. Chem. **172**, 108778 (2020). https://doi.org/10.1016/j.radphyschem.2020.108778
10. F. Akman, M.R. Kaçal, N. Almousa, M.I. Sayyed, H. Polat, Gamma-ray attenuation parameters for polymer composites reinforced with $BaTiO_3$ and $CaWO_4$ compounds. Prog. Nucl. Energy **121**, 103257 (2020). https://doi.org/10.1016/j.pnucene.2020.103257
11. K.M. Kaky, M.I. Sayyed, M.H.A. Mhareb, A.H. Abdalsalam, K.A. Mahmoud, S.O. Baki, M.A. Mahdi, Physical, structural, optical and gamma radiation attenuation properties of germanate-tellurite glasses for shielding applications. J. Non. Cryst. Solids. **545**, 120250 (2020). https://doi.org/10.1016/j.jnoncrysol.2020.120250
12. M. Rashad, A.M. Ali, M.I. Sayyed, H.H. Somaily, H. Algarni, Y.S. Rammah, Radiation attenuation and optical features of lithium borate glasses containing barium: $B_2O_3{\cdot}Li_2O{\cdot}BaO$. Ceram. Int. **46**, 21000–21007 (2020). https://doi.org/10.1016/j.ceramint.2020.05.165
13. I. Boukhris, I. Kebaili, M.S. Al-Buriahi, B. Tonguc, M.M. AlShammari, M.I. Sayyed, Effect of bismuth oxide on the optical features and gamma shielding efficiency of lithium zinc borate glasses. Ceram. Int. **46**, 22883–22888 (2020). https://doi.org/10.1016/j.ceramint.2020.06.061
14. M.Ç. Ersundu, A.E. Ersundu, N. Gedikoğlu, E. Şakar, M. Büyükyıldız, M. Kurudirek, Physical, mechanical and gamma-ray shielding properties of highly transparent ZnO-MoO_3-TeO_2 glasses. J. Non. Cryst. Solids. **524**, 119648 (2019). https://doi.org/10.1016/j.jnoncrysol.2019.119648
15. G. Lakshminarayana, Y. Elmahroug, A. Kumar, N. Rekik, D.E. Lee, J. Yoon, T. Park, Reckoning of nuclear radiation attenuation capabilities for binary GeO_2-Tl_2O, GeO_2-Bi_2O_3, and ternary GeO_2-Tl_2O–Bi_2O_3 glasses utilizing pertinent theoretical and computational approaches. Opt. Mater. (Amst). **108**, 110113 (2020). https://doi.org/10.1016/j.optmat.2020.110113
16. M.H.A. Mhareb, Y.S.M. Alajerami, N. Dwaikat, M.S. Al-Buriahi, M. Alqahtani, F. Alshahri, N. Saleh, N. Alonizan, M.A. Saleh, M.I. Sayyed, Investigation of photon, neutron and proton shielding features of H_3BO_3–ZnO–Na_2O–BaO glass system. Nucl. Eng. Technol. (2020). https://doi.org/10.1016/j.net.2020.07.035
17. M. Bengisu, Borate glasses for scientific and industrial applications: a review. J. Mater. Sci. **51**, 2199–2242 (2016). https://doi.org/10.1007/s10853-015-9537-4

18. K.A. Naseer, K. Marimuthu, M.S. Al-Buriahi, A. Alalawi, H.O. Tekin, Influence of Bi_2O_3 concentration on barium-telluro-borate glasses: physical, structural and radiation-shielding properties. Ceram. Int. (2020). https://doi.org/10.1016/j.ceramint.2020.08.138
19. E. Kavaz, F.I. El_Agawany, H.O. Tekin, U. Perişanoğlu, Y.S. Rammah, Nuclear radiation shielding using barium borosilicate glass ceramics. J. Phys. Chem. Solids. **142**, 109437 (2020). https://doi.org/10.1016/j.jpcs.2020.109437
20. M.G. Dong, O. Agar, H.O. Tekin, O. Kilicoglu, K.M. Kaky, M.I. Sayyed, A comparative study on gamma photon shielding features of various germanate glass systems. Compos. Part B Eng. **165**, 636–647 (2019). https://doi.org/10.1016/j.compositesb.2019.02.022
21. K.A. Naseer, P. Karthikeyan, S. Arunkumar, P. Suthanthirakumar, K. Marimuthu, Enhanced luminescence properties of Er^{3+}/Yb^{3+} doped zinc tellurofluoroborate glasses for 1.5 μm optical amplification. AIP Conf. Proc. **50**, 030237 (2020). https://doi.org/10.1063/5.0019171
22. K.A. Naseer, S. Arunkumar, K. Marimuthu, The impact of Er^{3+} ions on the spectroscopic scrutiny of Bismuth bariumtelluroborate glasses for display devices and 1.53 μm amplification. J. Non. Cryst. Solids. **520**, 119463 (2019). https://doi.org/10.1016/j.jnoncrysol.2019.119463
23. J.F. Briesmeister, *MCNP-a general Monte Carlo code for neutron and photon transport, version 4C* (National Laboratory, Los Alamos, 2000)
24. Q. Chen, K.A. Naseer, K. Marimuthu, P.S. Kumar, B. Miao, K.A. Mahmoud, M.I. Sayyed, Influence of modifier oxide on the structural and radiation shielding features of Sm^{3+}-doped calcium telluro-fluoroborate glass systems. J. Aust. Ceram. Soc. (2020). https://doi.org/10.1007/s41779-020-00531-8
25. S. Sindhu, S. Sanghi, A. Agarwal, V.P. Seth, N. Kishore, Effect of Bi_2O_3 content on the optical band gap, density and electrical conductivity of $MO{\cdot}Bi_2O_3{\cdot}B_2O_3$ (M = Ba, Sr) glasses. Mater. Chem. Phys. **90**, 83–89 (2005). https://doi.org/10.1016/j.matchemphys.2004.10.013
26. K.A. Naseer, K. Marimuthu, The impact of Er/Yb co-doping on the spectroscopic performance of bismuth borophosphate glasses for photonic applications. Vacuum (2020). https://doi.org/10.1016/j.vacuum.2020.109788
27. P. Suthanthirakumar, S. Arunkumar, K. Marimuthu, Investigations on the spectroscopic properties and local structure of Eu^{3+} ions in zinc telluro-fluoroborate glasses for red laser applications. J. Alloys Compd. **760**, 42–53 (2018). https://doi.org/10.1016/j.jallcom.2018.05.153
28. M.H.A. Mhareb, M.A. Almessiere, M.I. Sayyed, Y.S.M. Alajerami, Physical, structural, optical and photons attenuation attributes of lithium-magnesium-borate glasses: role of Tm_2O_3 doping. Optik (Stuttg). **182**, 821–831 (2019). https://doi.org/10.1016/j.ijleo.2019.01.111
29. V. Dimitrov, T. Komatsu, Optical basicity and chemical bonding of Bi_2O_3 containing glasses. J. Non. Cryst. Solids. **382**, 18–23 (2013). https://doi.org/10.1016/j.jnoncrysol.2013.10.005
30. D.P. Singh, G.P. Singh, Conversion of covalent to ionic behavior of Fe_2O_3–CeO_2–PbO–B_2O_3 glasses for ionic and photonic application. J. Alloys Compd. **546**, 224–228 (2013). https://doi.org/10.1016/j.jallcom.2012.08.105
31. Y.B. Saddeek, S.A.M. Issa, T. Alharbi, R. Elsaman, G. Abdelfadeel, A.M.A. Mostafa, K. Aly, M. Ahmad, Synthesis and characterization of lead borate glasses comprising cement kiln dust and Bi_2O_3 for radiation shielding protection. Mater. Chem. Phys. **242**, 122510 (2020). https://doi.org/10.1016/j.matchemphys.2019.122510
32. A. Makishima, J.D. Mackenzie, Direct calculation of Young's moidulus of glass. J. Non. Cryst. Solids. **12**, 35–45 (1973). https://doi.org/10.1016/0022-3093(73)90053-7
33. A. Makishima, J.D. Mackenzie, Calculation of bulk modulus, shear modulus and Poisson's ratio of glass. J. Non. Cryst. Solids. **17**, 147–157 (1975). https://doi.org/10.1016/0022-3093(75)90047-2
34. A. Abd El-Moneim, Analysis and prediction of elastic moduli and Poisson's ratio in Li_2O–B_2O_3–V_2O_5 glasses under the substitution of V_2O_5 for B_2O_3. Phys. Chem. Glas. Eur. J. Glas. Sci. Technol. Part B **60**, 146–156 (2019). https://doi.org/10.13036/17533562.60.4.001
35. C. Weigel, C. Le Losq, R. Vialla, C. Dupas, S. Clément, D.R. Neuville, B. Rufflé, Elastic moduli of $XAlSiO_4$ aluminosilicate glasses: effects of charge-balancing cations. J. Non. Cryst. Solids. **447**, 267–272 (2016). https://doi.org/10.1016/j.jnoncrysol.2016.06.023
36. U. Veit, C. Rüssel, Density and Young's Modulus of ternary glasses close to the eutectic composition in the CaO–Al_2O_3–SiO_2-system. Ceram. Int. **42**, 5810–5822 (2016). https://doi.org/10.1016/j.ceramint.2015.12.123
37. G. Scannell, L. Huang, T. Rouxel, Elastic properties and indentation cracking behavior of Na_2O-TiO_2-SiO_2 glasses. J. Non. Cryst. Solids. **429**, 129–142 (2015). https://doi.org/10.1016/j.jnoncrysol.2015.09.011
38. T. Rouxel, Elastic properties of glasses: a multiscale approach. Comptes Rendus Mécanique. **334**, 743–753 (2006). https://doi.org/10.1016/j.crme.2006.08.001

39. I.Z. Hager, Effect of Er_2O_3 and ErF_3 on the structural and elastic properties of sodium oxyfluoroborate glasses. J. Alloys Compd. **539**, 256–263 (2012). https://doi.org/10.1016/j.jallcom.2012.06.031
40. M.M. Smedskjaer, J.C. Mauro, S. Sen, J. Deubener, Y. Yue, Impact of network topology on cationic diffusion and hardness of borate glass surfaces. J. Chem. Phys. **133**, 154509 (2010). https://doi.org/10.1063/1.3497036
41. P. Kaur, K.J. Singh, M. Kurudirek, S. Thakur, Study of environment friendly bismuth incorporated lithium borate glass system for structural, gamma-ray and fast neutron shielding properties, Spectrochim. Acta Part A Mol. Biomol. Spectrosc. **223**, 117309 (2019). https://doi.org/10.1016/j.saa.2019.117309
42. M.J. Berger, J.H. Hubbell, XCOM: Photon Cross Sections Database, Web Version 1.2., MD 20899, Gaithersburg (1987)